AN ABSTRACT OF THE THESIS OF

Alex C. Misner for the degree of Master of Science in Nuclear Engineering presented

on October 21, 2005.

Title: Modeling Radiation and Hydrogen Production in a Radioisotope Micro-Power
Redacted for privacy
Source

Abstract approved: _____

Todd S. Palmer

Radioisotope based power systems have been used for several decades. This

research covers a new concept in the field, a radioisotope micro-power source (RIMS).

A RIMS cell consists of a radioactive source, a hydrogenous material, and a hydrogen

fuel cell.

The fuel cell is powered by hydrogen separated from the hydrogenous

material, in this case water, by the energy deposition of the particles emitted by the

radioisotope. This process is known as radiolysis. The amount of hydrogen produced

through radiolysis is determined by the G value of the hydrogenous material, which is

a function of that material's stopping power.

This thesis includes models of hydrogen production of various isotopes, the

self-shielding of source particles, the shielding effects of an infinite medium of

particles, the hydrogen production of a porous plate, and the hydrogen production of a

beam in a particle accelerator.

Modeling Radiation and Hydrogen Production in a Radioisotope Micro-Power Source

by

Alex C. Misner

A THESIS

submitted to

Oregon State University

in partial fulfillment of
the requirements for the
degree of

Master of Science

Presented October 21, 2005
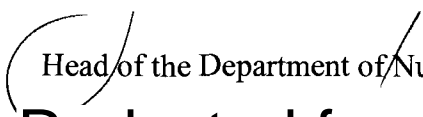Commencement June 2006

Master of Science thesis of <u>Alex C. Misner</u> presented on <u>October 21, 2005</u>

APPROVED:

Redacted for privacy

Major Professor, representing Nuclear Engineering

Redacted for privacy

Head of the Department of Nuclear Engineering and Radiation Health Physics

Redacted for privacy

Dean of the Graduate School

I understand that my thesis will become part of the permanent collection of Oregon State University libraries. My signature below authorizes release of my thesis to any reader upon request.

Redacted for privacy

Alex C. Misner, Author

ACKNOWLEDGEMENTS

I would like to thank my advisor, Dr. Todd Palmer, for the guidance and encouragement he has given me over the course of this research. I would also like to thank the other two faculty members that I worked with on this project, Dr. Qiao Wu and Dr. Andrew Klein. Finally I would like to thank my family and friends for the encouragement they have given me over the course of my education.

TABLE OF CONTENTS

TABLE OF CONTENTS (Continued)

TABLE OF CONTENTS (Continued)

Page

LIST OF FIGURES

LIST OF TABLES

MODELING RADIATION AND HYDROGEN PRODUCTION IN A RADIOISOTOPE MICRO-POWER SOURCE

1. Introduction

There is great interest in the area of miniaturization. The smaller a device can be made, the more options are available for its deployment. The military in particular is interested in the development of Micro Electro-Mechanical Systems (MEMS) to augment or replace current technology.

The MEMS technologies that are currently being used by the military are generally in the areas of guidance systems, navigation, and targeting. MEMS are used to provide attitude data on laser sites on armored vehicles. The unmanned aerial vehicle (UAV) Global Hawk uses a MEMS based accelerometer.

There are several areas that have potential for the expansion of MEMS technology for the military. It could be possible to develop a sensor that detects chemical agents that could fit into a button on a soldier's uniform. The army and navy are both planning to have guided artillery rounds enter service in the next two years. The army also plans to produce a guided mortar round in the next few years. All of those systems will use a MEMS inertial measurement unit for navigation.

With the increased use of miniature devices, the demand for miniature power supplies also increases. Ideally, these power sources would be integrated with the MEMS unit so that when it is added to a piece of military hardware the amount of connections that need to be made is minimized. However, if the power sources are

integrated, they have to have significant longevity to make the sensors cost effective. Current battery technology will not last for multiple years and would require the frequent replacement of any MEMS that they were integrated with.

One solution to a long-term, miniaturized power sources is the use of radioisotopes to generate electricity. There are three general categories of radioisotope-based power sources: those that directly use the decay particles to generate electricity, those that use the thermal energy release from decay, and those that use a secondary product of the radiation to generate electricity.

An example of a device that uses the particles that are emitted by radioactive decay to generate electricity is a β voltaic cell. This design is based on the ability of a β particle to create electron-hole pairs in a semiconductor that provide a current when placed under a bias. These devices provide thousands of times greater energy density than lithium-ion chemical batteries (Lal and Blanchard, 2004). Some of the challenges for this type of device are the inherent damage that the process does to the semiconductor by dislocating atoms in the lattice structure of the material and the relatively low conversion efficiency of 4%.

Devices that use the thermal energy released by radioactive decay are the most mature technology of the three categories. NASA has a long history of using radioisotope thermal generators (RTGs) on spacecraft and experiment sets. The projects that have used these devices range from the Apollo lunar landings to the Cassini orbiter currently exploring the Saturn system. RTGs are valuable for any probe that travels to the outer solar system where the light of the sun is too faint to

power solar cells. The challenge of adapting these devices to power MEMS is that they do not scale down well with size (Lal and Blanchard, 2004).

A device that uses a secondary product of radioactive decay emissions is a radiolysis cell. This is the type of device that is the focus of this thesis. These devices depend on the ability of radiation to break water molecules into hydrogen and oxygen and then using the hydrogen produced to power a hydrogen fuel cell. This design has several advantages: when hydrogen is run through a fuel cell, it recombines with oxygen to form water, thereby creating a closed fuel cycle for this device; because the radiation has a relatively short range, it is possible to design the cell so that all of the radiation is absorbed in the water and therefore cannot cause damage to the fuel cell itself; these devices also have the potential to have a greater efficiency than is seen in semiconductor-based devices. In order to design and build one of these devices, several key questions must be answered.

First, an isotope has to be chosen to power the cell. There are many isotopes that could be used and they have vastly different properties. The isotopes fall into 2 general categories: α emitters and β emitters. The two types have different hydrogen production potential, half-lives, and health concerns.

Second, a geometry has to be decided for the source material. There are a multitude of options ranging from colloidal suspensions to solid plates. This research focuses on the two cases of nanoparticles and porous plates. In order to gauge the effectiveness of the geometries, analysis must be performed on the optimal size of the nanoparticles and the porosity of the plate. Figure 1.1 shows the geometry of a RIMS cell that utilizes a porous plate source configuration.
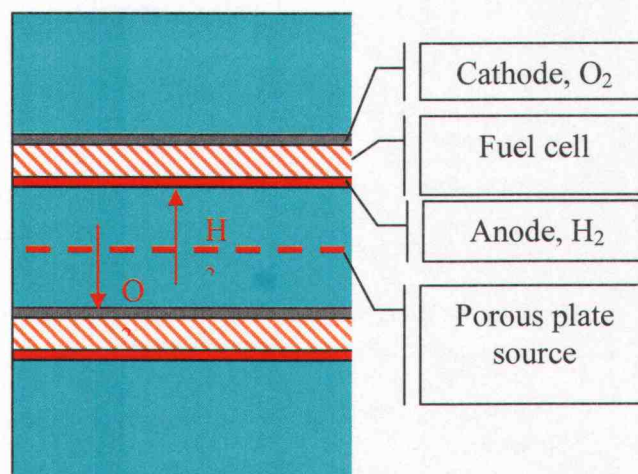
Figure 1.1: RIMS cell geometry utilizing a porous plate source

Third, the hydrogen production must be modeled for a given source configuration. It is important to understand the spatial distribution of the creation of the hydrogen so that it can be used as an input to a model for the transport of the hydrogen to the fuel cell.

Finally, the health risks of the radioactive material used in the cell has to be assessed. Any radiation has the potential to produce a biological hazard if the exposure level is too high. There are levels of dose that cannot be exceeded by any source used in the RIMS.

The remainder of this thesis is organized in the following way. In section 2, background is given for the project in general and in the physics of the processes examined in this research. Section 3 details the methods that were used to obtain the data for this study. The results of the models are detailed in section 4. Section 5 contains the data and analysis relating to the dose received from a RIMS cell. Section 6 contains the discussion of the results of the study and the future work that is required to complete the RIMS cell. Appendix A contains a commented MCNPX input deck

used in this study and appendix B details a visualization program developed to aid in

the interpretation of the MCNPX output.

2. Background

This section will provide the necessary information on the underlying principles used to address the objectives of this thesis. Those objectives are to select an appropriate source isotope, model the self-shielding effects of the source geometry, and model the hydrogen production process in the cell. All of these objectives are based on the physics of radiation and its interaction with matter. The hydrogen production in this cell is based on the process of radiolysis which is in turn based on the physics of stopping power. Several of the models used utilize a tool that uses the Monte Carlo method for particle transport, so information about that method is also provided.

2.1 Nuclear Radiation Background

Nuclear radiation is the phenomenon of particles being released from the nuclei of atoms. Radiation generally occurs when a nucleus transforms itself from an unstable state to a stable one. The four basic types of nuclear radiation are α, β, γ, and neutron.

2.1.1 α Particles

α particles are the heaviest of the common radiation types. They are ^{4}He nuclei, consisting of two protons and two neutrons. They also tend to be higher in energy than either β or γ emissions, with energies ranging from 4 to 6 MeV. α emitters are generally nuclei with more than 82 protons. Due to their charge of +2, αs interact strongly with the electron shells of the atoms in the media that they move

through. This causes α particles to transfer their energy quickly, which translates to a short range. α particles do not deposit their energy uniformly along their path, but rather release most of it at the very end of their track. This upward spike in the energy deposition is known as the Bragg peak. Figure 2.1 shows the Bragg peak of a 4.5 MeV α particle.
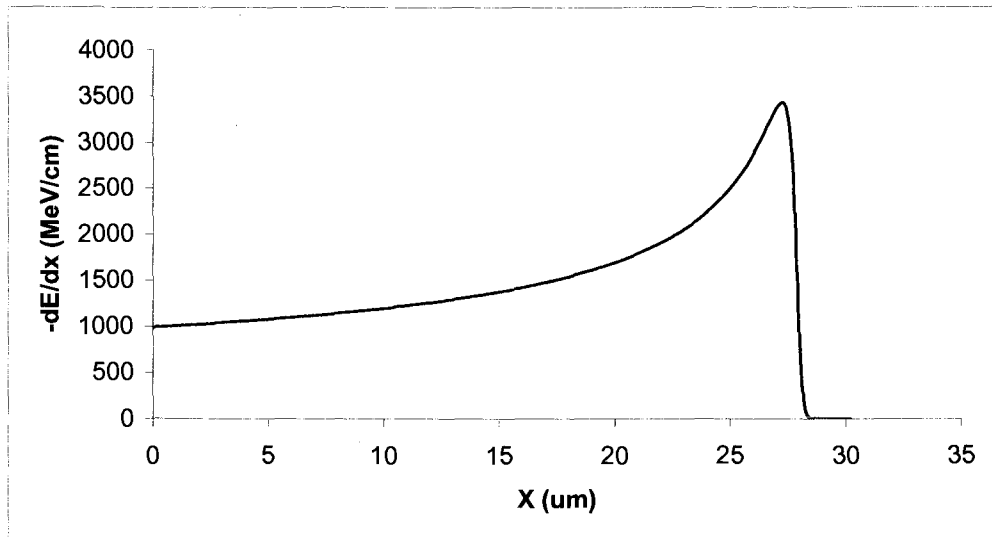
Figure 2.1: Bragg peak of a 4.5 MeV α particle

2.1.2 β Particles

β particles are much lighter than α particles, being either electrons or positrons. Unlike α particles, β particles are emitted by nuclei across the complete range of masses from hydrogen isotopes to actinides. β particles are released when nucleons change types through an interaction via the weak nuclear force. Equations 2.1 and 2.2 show the reaction that releases a β⁻ and a β⁺, respectively.

$$n \rightarrow p + \beta^- + \bar{\nu} \tag{2.1}$$

$$p \rightarrow n + \beta^+ + \nu \tag{2.2}$$

ν is a neutrino in the above equation and a bar over a symbol denotes an anti-particle. Because the neutrinos are emitted in the same event as the β particles, they also share

in the energy released in the decay. This causes β particles to be emitted as a continuous spectrum of energy rather than the discrete energies at which α particles are emitted. As a rule of thumb, the average energy of β particles emitted by an isotope is one third of the maximum energy of a β particle emitted by that nucleus.

2.1.3 γ Rays

γ rays are photons rather than massed particles. They are electromagnetic emissions with energies greater than X-rays. Nuclei emit γs when they fall to an unexcited state in a phenomenon similar to electrons falling to lower shells and emitting photons. Nuclei become excited through either absorbing another particle or by emitting another type of radiation. Because of this, γs generally accompany the other types of radioactive emissions. γ rays have much longer ranges than either αs or βs, but like those types of particles, usually interact with the electron shells of the media that they move through.

There are three primary ways that a γ can interact with material: Compton scattering, the photoelectric effect, and pair production. Compton scattering occurs when the γ knocks an outer electron out of an atom and continues to move through the material. The photoelectric effect is when a γ transfers all of its energy to an interior electron, causing that electron to be ejected from the atom. The photon is destroyed in the photoelectric effect. Pair production occurs when a high-energy γ passes through the magnetic field of a nucleus and spontaneously splits into a particle and its antiparticle. The minimum energy required for this interaction is double the rest energy of the particle that is created in the reaction.

2.1.4 Neutrons

Neutrons are subatomic particles with no electrical charge. They lose their energy through scattering or absorption reactions. Because they have no charge, the nucleus is the only part of the atom that they interact with, which makes them more difficult to shield than the other types of radiation.

For a shield to be effective, it has to absorb the neutrons. The probability of being absorbed, which is called the absorption cross-section, is generally inversely proportional to the energy of the neutron. Thus, neutron shields often include materials with light nuclei that slow neutrons down when they collide with them.

Neutrons are usually emitted as a result of absorption or fission reactions. In particular, several isotopes have non-negligible (α,n) cross-sections. Figure 2.2 shows an (α,n) reaction with oxygen.
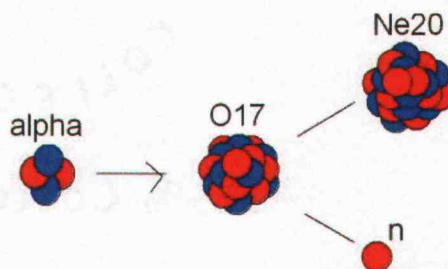
Figure 2.2: The (α,n) reaction with an isotope of oxygen

2.2 Radiolysis Background

Radiolysis is the process of radiation causing the release of materials that are constituents of a medium. The physics behind the process of radiolysis is that some of the energy deposited by radiation in a medium is consumed by breaking chemical bonds in that medium. In the case of this research, the medium is water and the

material of interest is hydrogen. The understanding of the process of radiolysis is key to this research.

Any type of radiation can cause radiolysis, so a factor has been developed to describe radiolysis that is independent of the particle type. That factor is called the G value, which has units of amount of material released per unit of energy deposited in the medium. The G value is a function of linear energy transfer, also called stopping power

Stopping power is a quantity that describes the amount of energy transferred from a particle to a medium per unit distance traveled in the medium. Hans Bethe developed equations that fit experimentally determined stopping powers for both electrons and heavy charged particles (Krane). Equation 2.3 is the expression for stopping power for electrons and Equation 2.4 is the expression for heavy charged particles.

$$-\left(\frac{dE}{dx}\right) = \frac{\varepsilon_0^2 e^4 n}{4\pi m_0 c^2 \beta^2}\left[\ln\left(\frac{m_0 c^2 \tau \sqrt{\tau+2}}{I\sqrt{2}}\right) + \frac{1-\beta^2}{2}\left[1 + \frac{\tau^2}{8} - (2\tau+1)\ln 2\right]\right] \qquad (2.3)$$

$$-\left(\frac{dE}{dx}\right) = \frac{\varepsilon_0^2 z^2 e^4 n}{4\pi m_0 c^2 \beta^2}\left[\ln\frac{2m_0 c^2 \beta^2}{I\left(1-\beta^2\right)} - \beta^2\right] \qquad (2.4)$$

Table 2.1 shows the variables and constants used in equations 2.3 and 2.4.

Table 2.1: Symbols Used in Stopping Power Equations

Symbol	Meaning
ε_0	Permittivity of free space
z	Atomic number of incident particle
e	Charge of an electron
n	Electron density of medium
m_0	Rest mass of an electron
c	Speed of light in a vacuum
β	Velocity of incident particle as a fraction of speed of light in a vacuum
I	Mean excitation energy of medium
τ	Kinetic energy of incident particle as a fraction of rest energy

Figures 2.3 and 2.4 Show the plots of stopping power for alpha and beta particles in water, respectively.
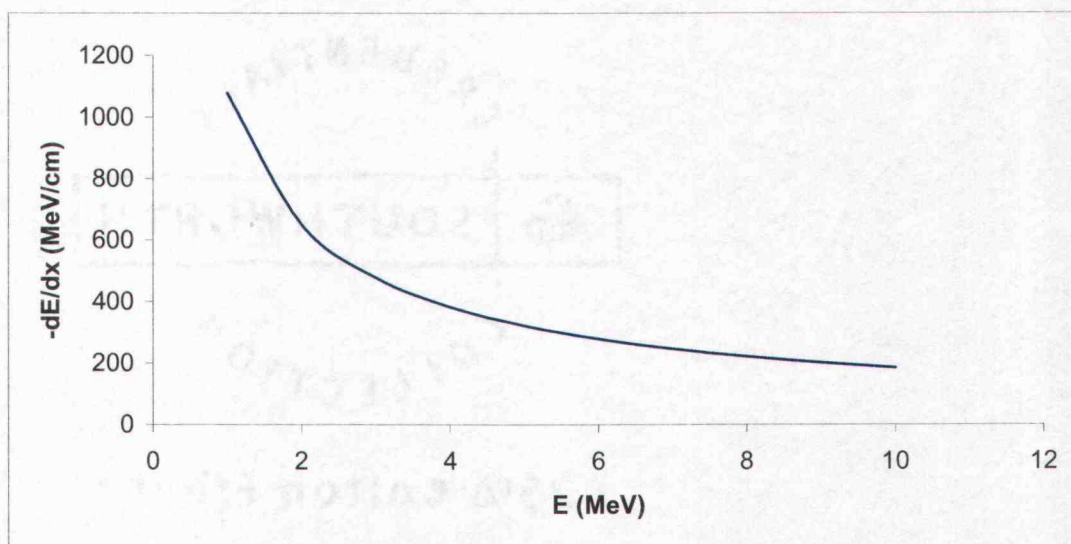
Figure 2.3: Plot of α particle stopping power in water
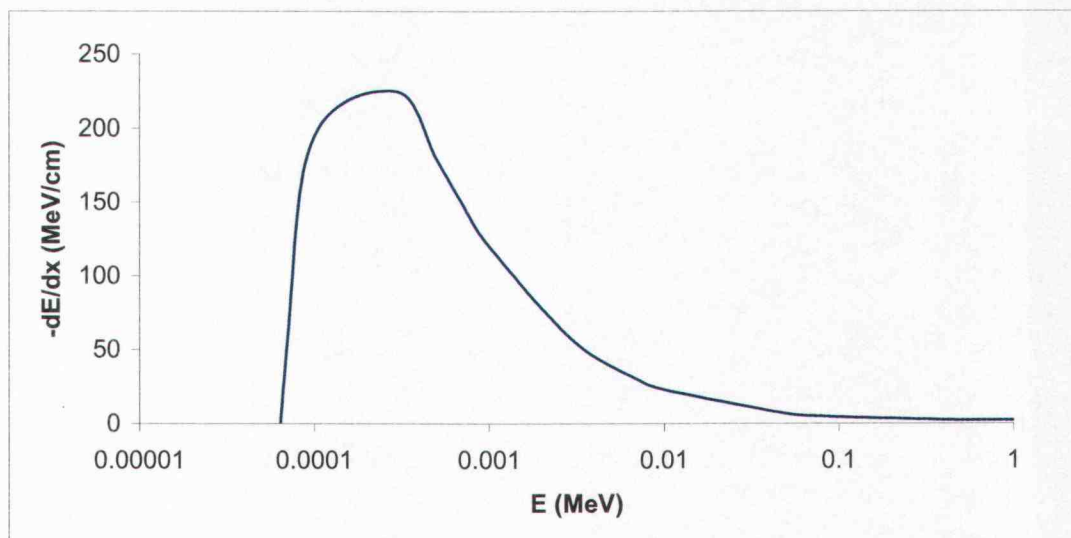
Figure 2.4: Plot of β particle stopping power in water

The function for the G value for molecular hydrogen produced from water was obtained by performing a curve-fit analysis on experimental data (Allen). Figure 2.5 is the plot of the G value with a power function trend line applied to it.

$y = 0.0323x^{0.2189}$

$R^2 = 0.9906$
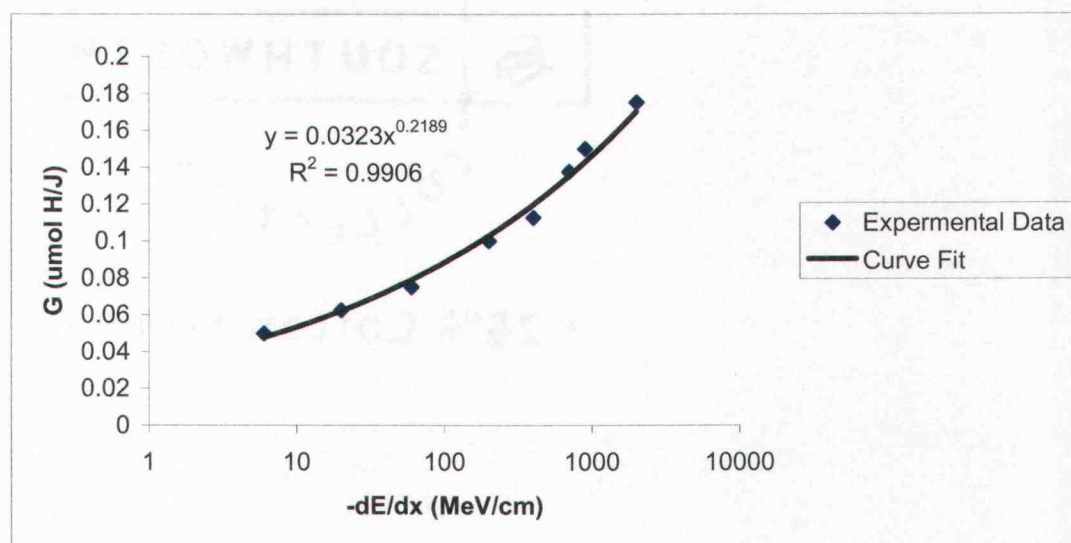
Figure 2.5: Plot of the G value for molecular hydrogen production from water with power function trend line applied

Vinson, Deible, and Sindelar (2002) studied the hydrogen production due to breached spent fuel. They found that different types of radiation have different effects on the net hydrogen production rate. The study concluded that X-rays, γ rays, and β particles increase the rate of recombination of hydrogen by creating free radicals, depressing the net production rate. Conversely, α particles were shown to cause a net breakdown of the water solution. It was shown that the presence of boric acid in solution with the water also caused a net increase in hydrogen production by releasing additional α particles through an (α, n) reaction.

Hydrogen production in boric acid solutions was also studied by Hart, McDonell, and Gordon (1956). This study examined the process of radiolysis in both heavy and light water reactors. It was found that a light water solution produced more hydrogen at a given concentration of boric acid than a heavy water solution. The study also determined that the addition of potassium iodide or hydrogen peroxide would also increase the rate of hydrogen production. This increase in hydrogen production can be interpreted as an increase of the G value of the solution.

Dolin and Ershler (1956) examined the process of hydrogen production in heavy water reactors. Among the variables tested, the study examined the influence of chemicals placed in the water on the hydrogen production rate. It was found that the additions of HCl, H_2SO_4, and KOH to the water increased the hydrogen production rate. The study also showed that the presence of metal impurities in the water could boost the production of hydrogen up to a certain water temperature, above which the impurities would suppress the radiolysis process. The authors found that an increase

in temperature of 200°C reduced the saturation pressure of hydrogen in the water and therefore lessened the rate of radiolysis.

Crawford and Bibler (1995) investigated the effect acidity had on the G value of a slurry. The two slurries that were studied were potassium tetraphenyl borate (KTPB) and polyhydroxy acid (PHA). The acid solution showed a twofold increase in G value over the other slurry.

It is of note that the above studies were focused on minimizing hydrogen production through radiolysis. In the current study, the goal is to maximize the hydrogen production rate.

2.3 Monte Carlo Background

The Monte Carlo method is one that samples probability distribution functions to describe a physical process. When applied to particle transport, this involves tracking a particle from its birth at the source until its death by absorption, escape, or some other means.

For the research on the OSU RIMS project, the Monte Carlo code that was used was MCNPX. MCNPX is a modification of the Monte Carlo N-Particle code that was developed by Los Alamos National Laboratory. In the cases of MCNP and MCNPX, the random samples used to build up the predictions are particle histories. A particle history is all of the events a particle undergoes between its birth and its death. A particle is born either through radioactive emission, a collision event, or a fission event. Particles are considered to die when they leave the geometry defined for the

problem, they are absorbed, or if their energy falls under the cut off set for the problem. (Waters 2002)

The events that make up the histories are simulated based on cross-sections. Cross-sections for particle interaction are not based solely on geometric size, but rather by the probability of an interaction occurring. They are dependent on particle type, the energy of the incoming particle, and the change of direction experienced by the particle.

MCNP and MCNPX allow a user to define the geometry, materials, and source information for a given problem and specify output quantities through the use of tallies. Tallies are objects that count the events that occur at a point, over a surface, or within a volume cell that are related to various user defined quantities. Quantities that can be tallied include current, flux, energy deposition, and charge deposition.

The largest distinctions between MCNPX and MCNP are the types of particles that the codes can transport and the energy range of the particles. MCNP can transport neutrons, photons, and electrons, whereas MCNPX can handle a total of 34 particles including protons and alpha particles. MCNPX also has the added capability of using mesh tallies. Mesh tallies are essentially three dimensional arrays of volume tallies overlaid onto the defined geometry. The advantage of using mesh tallies over traditional tallies is that the results of mesh tallies can be converted into a format that can be displayed in a number of plotting programs.

Based on the plot of the G value, it is clear that the key to maximizing the hydrogen production in the RIMS cell is to find an isotope that emits a particle to which water has the maximum stopping power. The physics dictates that an α emitter

would fit this role. The physics also show that neutrons will be the largest problem from a health stand point due to the fact that they will not be able to be shielded in such a small volume.

3. Methods

This chapter discusses the methodology used for the modeling of the RIMS cell. Figure 3.1 is a flow chart of the general model of the device.
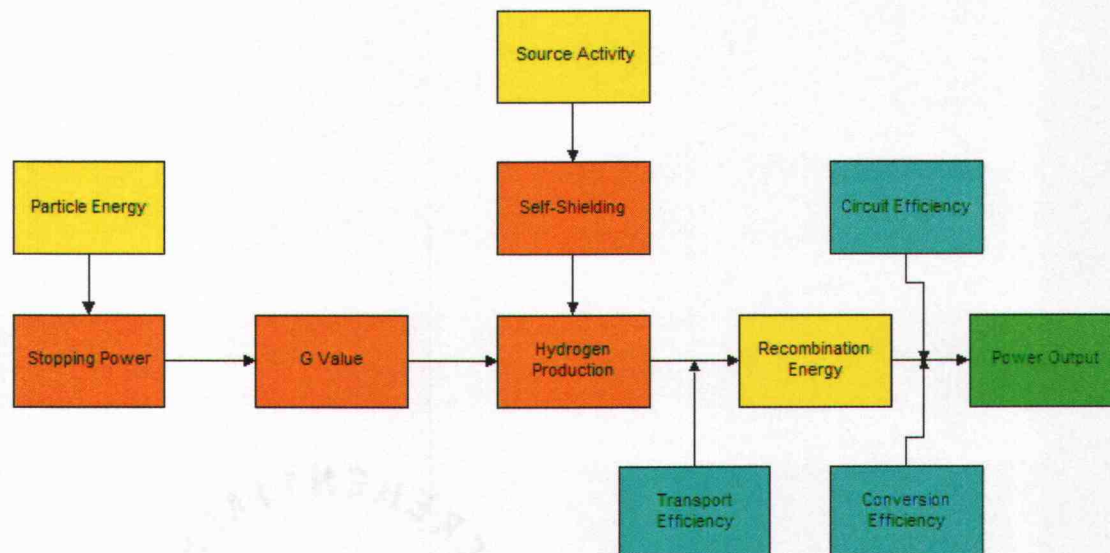
Figure 3.1: Flow chart of the general system model for the OSU RIMS cell

In the above figure, the boxes are color coded by category. The yellow boxes represent known values, aqua boxes represent assumed numerical values, the green box is the final output, and the orange boxes are the primary focus of this thesis.

3.1 Self-Shielding

The self-shielding for the sources in the RIMS cell can be divided into two causes: particle size and particle spacing. The shielding due to particle size is the energy that is absorbed inside of a source particle rather than be absorbed in the surrounding medium. The shielding due to the particle spacing is the energy that is absorbed by neighboring source particles rather than the surrounding medium. Both of these problems were modeled using MCNPX.

3.1.1 Particle Size

To model the energy loss in the source particle itself, a simple MCNPX geometry was used. The geometry consisted of a spherical particle of plutonium oxide in a vacuum. Tallies for α particle current and α energy current were placed on the surface of the sphere and a tally for energy deposition was placed in the volume of the sphere. An uniform α particle source was placed in the volume of the sphere.

Dividing the result of the α energy current tally by the α particle current gives the average energy of the α particles leaving the source sphere and entering the surrounding medium. This can be used as the input for models of hydrogen production.

The diameter of the source sphere was varied from 20 nm to 20000 nm and the source strength was adjusted for the appropriate mass of plutonium.

3.1.2 Particle Spacing

The issue of particle spacing is more complicated than that of the shielding due to the particle itself. The geometry used for this model consisted of a cube of water with reflective boundary conditions on each side. In each corner of the cube, an eighth of a sphere of plutonium oxide was placed. This represents an infinite medium of plutonium oxide spheres in water.

An uniform α source was placed in the volume of one of the spheres and tallies for energy deposition were placed in all of the non-source spheres. An energy current tally was placed on the surface of the source sphere. The fractional energy loss can by

calculated by dividing the sum of all of the energy deposition tallies by the total energy released by the source particle.

The particle sizes in these models included 1 μm, 3 μm, 10 μm, and 30 μm. The concentration of plutonium oxide in the water was varied from 0.05 g/cc to 0.5 g/cc.

3.2 Stopping Power Modeling

The stopping power for the sources was modeled using two methods. One method used was through mesh tallies in MCNPX that directly measure stopping power. The second method was using a spread sheet to calculate stopping power using formulas 2.3 and 2.4 for β particles and heavy charged particles, respectively.

3.3 Hydrogen Production Modeling

The model of hydrogen production in the RIMS cell involved combining two types of data: stopping power and energy deposition. The stopping power data was obtained through the methods described in section 3.2 and the energy deposition was found in a similar manner.

For the energy deposition, two methods were used. The first method was using mesh tallies for energy deposition to directly simulate this data. The second method was by using a spread sheet to calculate the energy lost by a particle in a medium with a given stopping power over a known distance.

Once the stopping power is known, the G value can be calculated. Equation 3.1 is the formula for the curve fit of the G value data for molecular hydrogen in water that is shown in Figure 2.5.

$$G = 0.0323 \left(-\frac{dE}{dx} \right)^{0.2189} \tag{3.1}$$

The hydrogen production in µmol H_2 can then be calculated by multiplying the result of Equation 3.1 by the energy deposition in Joules. By combining this data with the knowledge of how many particles pass through the region in a second, the hydrogen production rate can be obtained. This data is built into the MCNPX results, which have an implied per second in their units. It is simulated in the spread sheet models by multiplying the hydrogen production number by the activity of the source.

4. Results

In this chapter, the results of the study will be presented. The results are divided into the categories of source modeling and case studies performed to answer specific questions.

4.1 Source Modeling

The problem being investigated in the source models is the effect the source geometry has on the particles that are emitted. There are two geometric concerns: the shielding due to the material in the source particle itself and the amount of energy that is radiated by the source particle that is then absorbed by the neighboring source particles.

4.1.1 Particle Size

The data for the particle size analysis was calculated with a combination of MCNPX and Excel. The tallies for current, energy current, and energy deposition in the plutonium spheres were used to calculate the average energy of the α particles and the amount of energy that was deposited in the surrounding water per α generated by the source. Table 4.1 shows the data that was calculated in the particle size analysis.

Table 4.1: Data calculated in the particle size analysis. The data was obtained from MCNPX

D (nm)	Current (# α)	E Current(MeV/s)	EinPu	Avg E	EinH2O/α
20	2.73500E-05	1.50350E-04	7.62E-08	5.497258	5.497214908
50	4.27380E-04	2.34760E-03	2.96E-06	5.493004	5.493077613
100	3.41900E-03	1.87570E-02	4.73E-05	5.486107	5.486153764
200	2.73520E-02	1.49680E-01	0.000757	5.47236	5.472313962
500	4.27380E-01	2.32100E+00	0.029584	5.430764	5.43077847
1000	3.41910E+00	1.83230E+01	0.47433	5.359013	5.361268555
2000	2.73520E+01	1.42620E+02	7.6998	5.214244	5.218496517
5000	4.27380E+02	2.03380E+03	311.87	4.758763	4.770277223
10000	3.41910E+03	1.33760E+04	5345.1	3.912141	3.936671843
20000	2.00270E+04	6.46200E+04	84493	3.226644	2.410949142

Figures 4.1, 4.2 and 4.3 show the α current, the average energy of α particles leaving the sphere, and the energy deposited in the water per α generated as a function of sphere diameter, respectively. Figure 4.4 shows the effects of self-shielding of the nanoparticles as percent of radiated energy deposited in the source sphere as a function of sphere diameter.
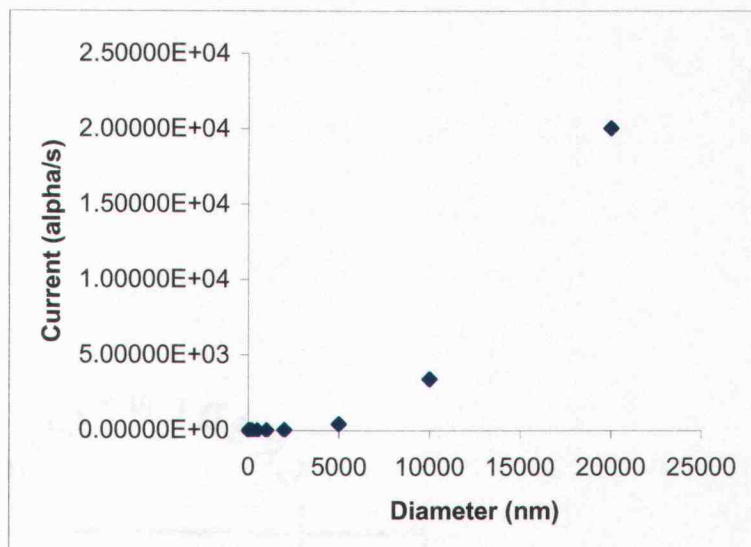
Figure 4.1: Outgoing α current as a function of plutonium oxide sphere diameter
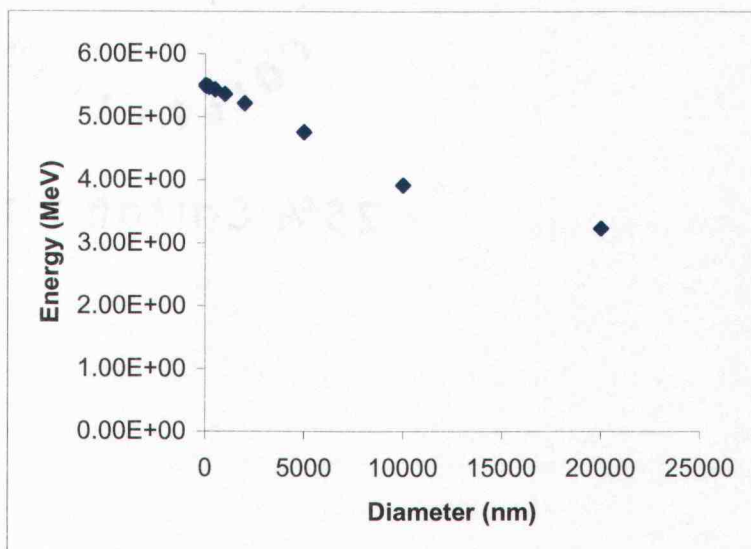
Figure 4.2: Average energy of outgoing α particles as a function of plutonium oxide sphere diameter
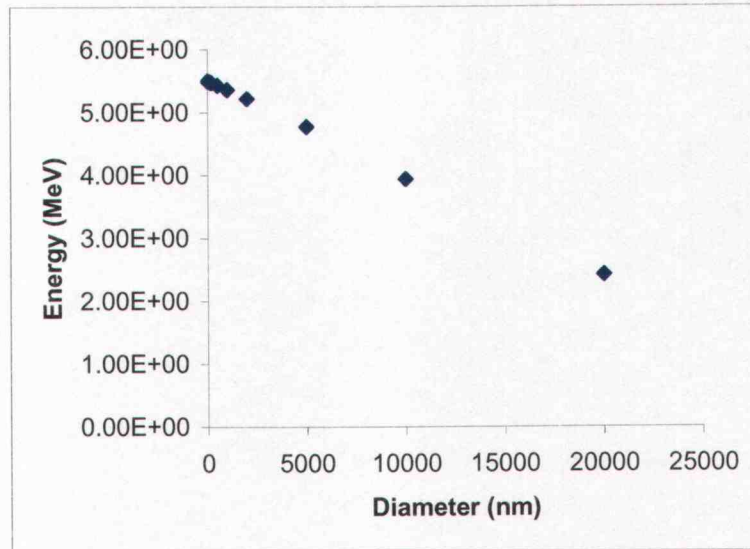
Figure 4.3: Energy deposited in surrounding water per α generated as a function of plutonium oxide sphere diameter
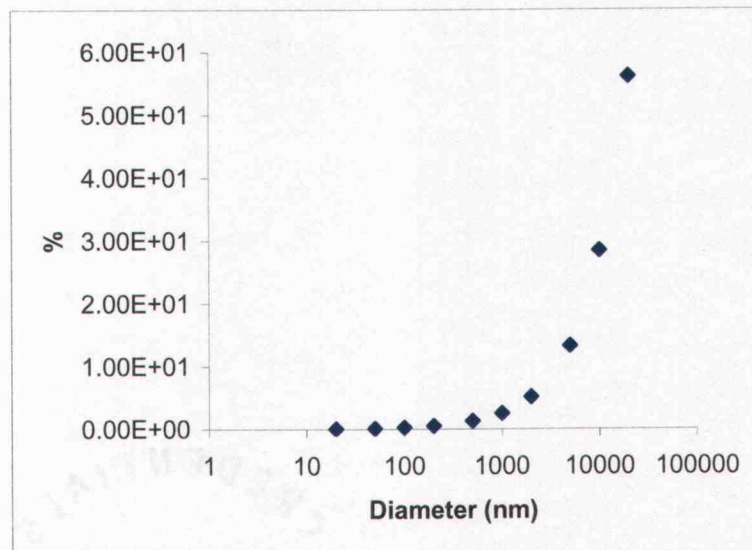
Figure 4.4: Self-shielding of nanoparticles shown as percent energy deposited in a plutonium oxide sphere as a function of sphere diameter

4.1.2 Particle Spacing

The data for the particle spacing analysis was calculated using MCNPX. The cases that were modeled varied the particle size while holding the mass concentration of plutonium oxide in the water constant. Figure 4.5 is a plot of the results. A case

using 30 μm spheres was modeled, however no α particles were measured to have

been absorbed by neighboring particles in that case.
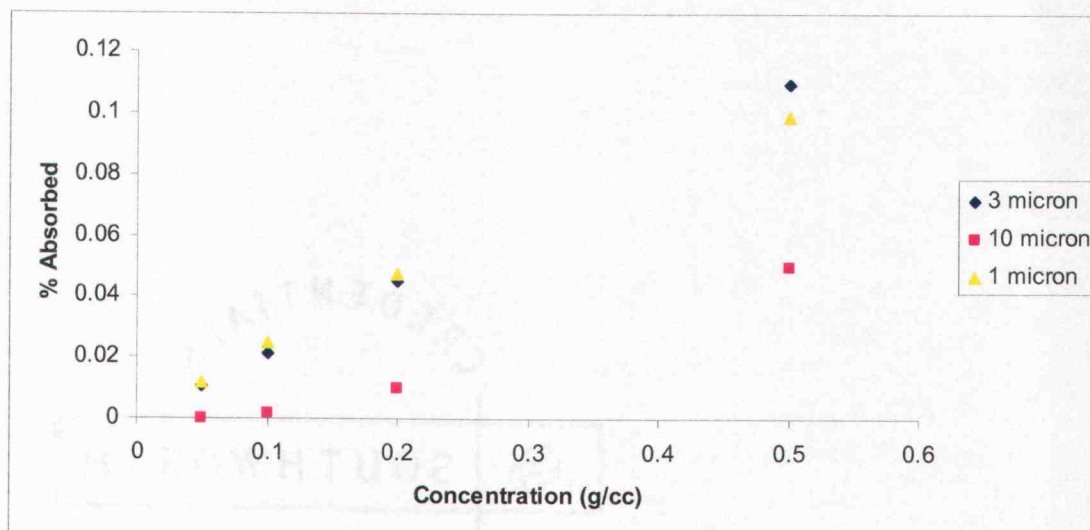
Figure 4.5: % Energy from α emission absorbed by neighboring PuO₂ particles as a function of PuO₂ concentration in water.

Table 4.2 is a the data displayed in Figure 4.5.

Table 4.2: % Energy from α emission absorbed by neighboring PuO₂ particles

Particle Size	0.05 g/cc	0.1 g/cc	0.2 g/cc	0.5 g/cc
1 μm	0.0118	0.0248	0.0473	0.0989
3 μm	0.010567	0.021482	0.044718	0.10956
10 μm	0	0.001793	0.010025	0.049911

4.2 Case Studies

There were 3 cases that were investigated for hydrogen production. The first

was a simple spread sheet model that was used to determine the most suitable source

isotope for the RIMS cell. The second was used to determine if a particle accelerator

could substitute for a radioactive source in hydrogen production experiments. The

third was an investigation of how the plutonium content of a thin porous plate affects

the hydrogen production rate.

4.2.1 Source Selection Model

The source selection model consisted of a simple spread sheet. There were 13 isotopes that were investigated, 6 α emitters and 7 β emitters. The model calculated the stopping power, hydrogen production rate, and mass of source material required to produce 10 mW of power for each isotope. The model assumed that all of the energy was lost in a single interval with the stopping power being held constant. This does not simulate the spatial distribution of the hydrogen production. This model also assumed that the efficiency of the hydrogen transport, fuel cell conversion, and circuitry was 100%.

Before this model was constructed, the only source selection model was a calculation provided by PNNL. That calculation assumed that all of the power that was emitted by the radioactive decay of the source material was converted to electricity.

The results of the source selection model provided key insights into the effectiveness of different isotopes to produce hydrogen. The primary trend that the model showed was that by including the G value in the electric power estimation, the estimate for the amount of source material required for 10 mW is significantly greater than that provided by calculating the decay power alone.

Tables 4.3 and 4.4 show the hydrogen production rates for the α emitters and β emitters, respectively.

Table 4.3: α emitter hydrogen production rates

Nuclide	Act.(Bq/g)	umol H/s/g
^{238}Pu	6.3344E+11	0.0788384
^{208}Po	2.1945E+13	2.575036
^{148}Gd	1.1988E+12	0.0940754
^{210}Po	1.6626E+14	20.09761
^{240}Pu	8.3990E+09	0.0009943
^{242}Cm	1.2252E+14	16.690689

Table 4.4: β emitter hydrogen production rates

Nuclide	Act (Bq/g)	umol H/s/g
^{3}H	3.5757E+14	0.0239288
^{90}Sr/^{90}Y	5.1578E+12	0.0345601
^{147}Pm	3.4299E+13	0.0160793
^{204}Tl	1.7153E+13	0.0259886
^{63}Ni	2.0979E+12	0.001049
^{14}C	1.6502E+11	0.0001724
^{39}Ar	1.2617E+12	0.0042852

Figure 4.6 is a plot comparing the initial mass requirement for the isotopes investigated to provide 10 mW and the masses predicted by the mono-energetic model.
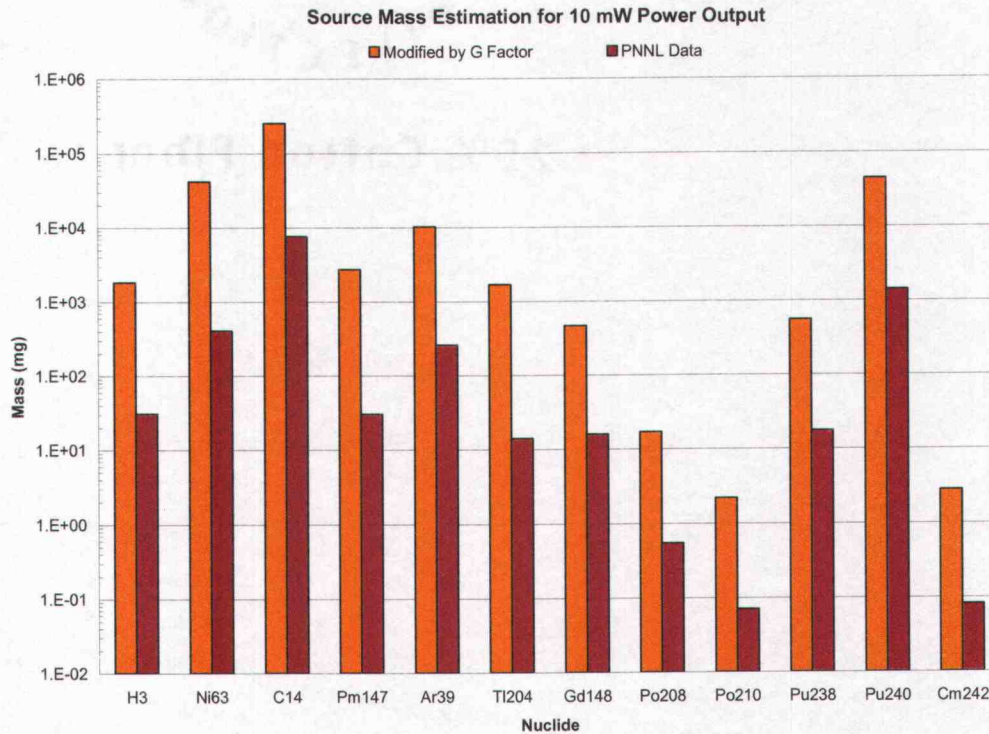
Figure 4.6: Source mass comparison of results from PNNL's decay power calculation and mono-energetic hydrogen production model

Figure 4.7 is a plot of a reduction of power production of α emitters due to radioactive decay of the source. The source was assumed to initially have the mass required to produce 10 mW.
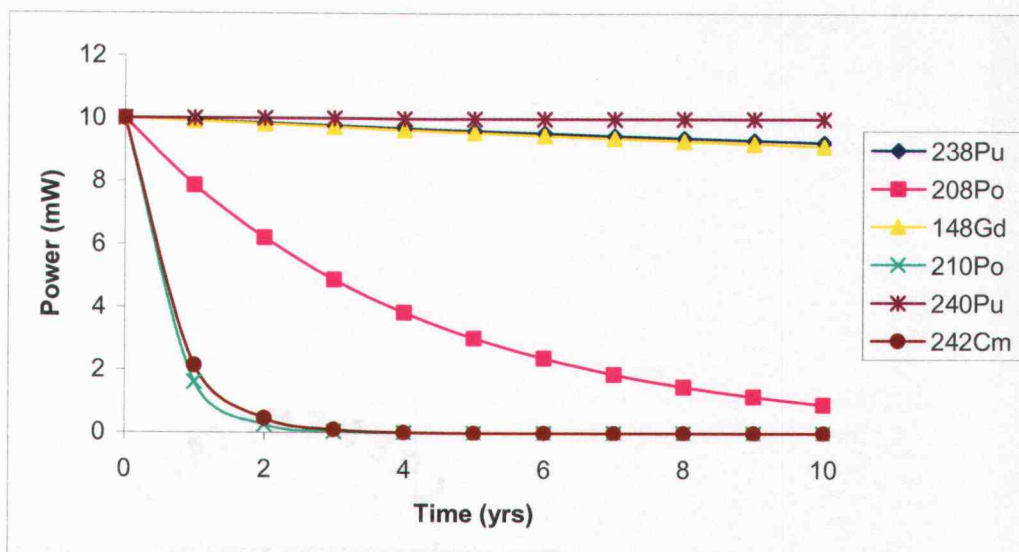
Figure 4.7: Change in power production from α emitting isotopes due to radioactive decay of the source material as a function of time

Figure 4.8 is a plot of the change in power production from β emitters due to the radioactive decay of the source material.
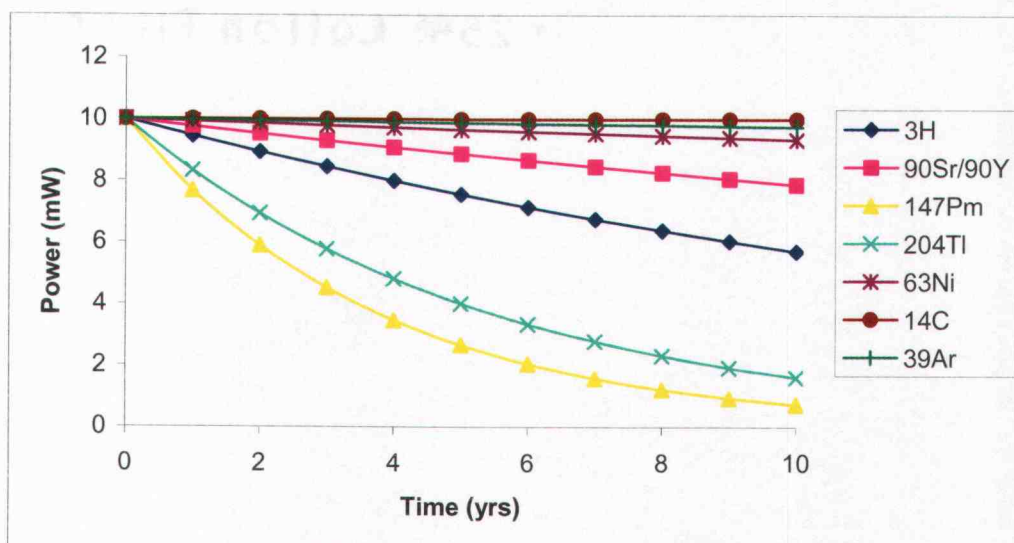
Figure 4.8: Change in power production from β emitting isotopes due to radioactive decay of the source material as a function of time

4.2.2 Accelerator Model

The particle accelerator model provided the initial proof-of-concept for using MCNPX to model hydrogen production. The model geometry consisted of a silicon carbide window with a water block behind it. A beam source was placed on the surface of the window with the particle type and particle current that are dictated by the particular case. The accelerator facility has the capability to produce α and proton beams. The cases modeled were a 2.5 MeV α beam, a 2.5 MeV proton beam, and a 5 MeV proton beam.

The accelerator model results showed the expected Bragg peak behavior and range for the particles that were modeled. This provided verification that the models were reflecting the physics of the problem.

Figure 4.9 is a plot of hydrogen production as a function of distance in water in the a 100 nA, 2.5 MeV α particle beam.
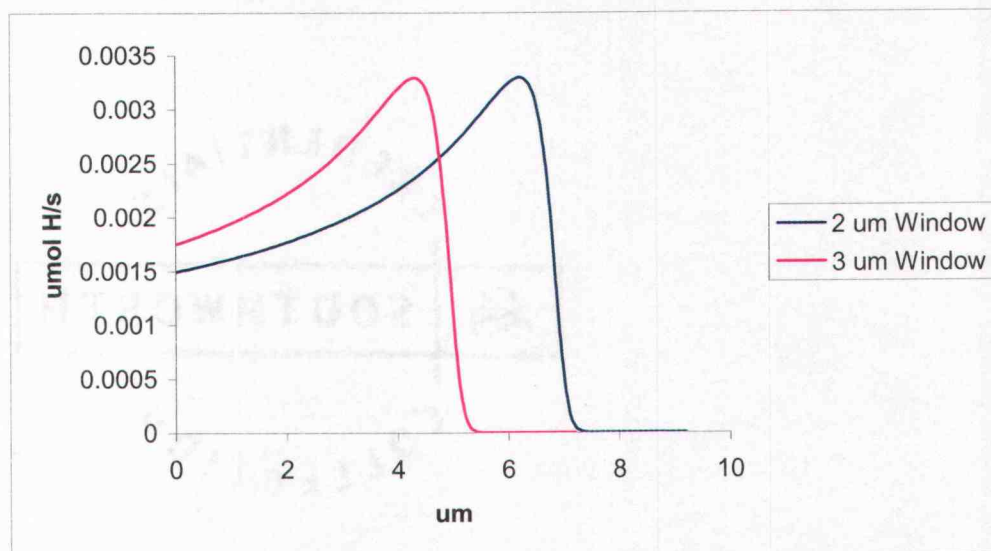
Figure 4.9: Hydrogen production as a function of distance in water for a 100 nA beam of 2.5 MeV α particles based on the Bethe model of stopping power

Figure 4.10 is a plot of hydrogen production as a function of distance in water for a 100 nA beam of protons.
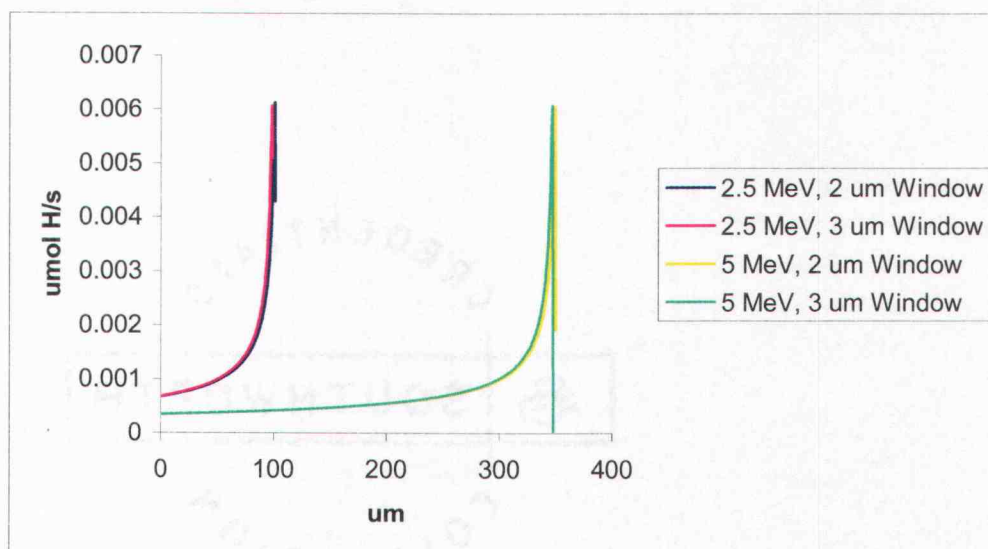
Figure 4.10: Hydrogen production as a function of distance in water for a 100 nA beam of protons based on the Bethe model of stopping power

The shape of the beam was also investigated and the beam was found to remain collimated in the water. Figure 4.11 is a contour plot made in HYPR of hydrogen production of a 2.5 MeV proton beam that illustrates the lack of beam divergence.
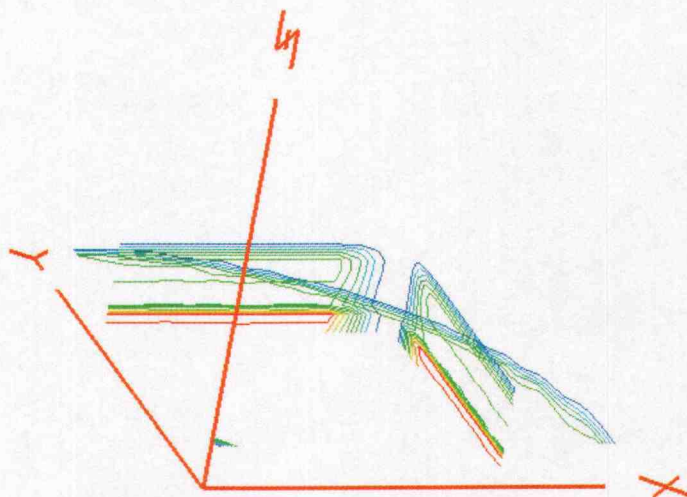
**Figure 4.11: Contour plot made in HYPR of hydrogen production of a 2.5 MeV proton beam. The data was obtained from MCNPX mesh tallies**

The investigators at CWRU were interested in how much of the beam energy would be lost before it interacts with the water. Table 4.5 shows the percent of energy deposition of the beam in the silicon carbide window.

Table 4.5: Percent of energy deposited in a silicon carbide window by particle beams in a linear accelerator

Particle Type	Energy (MeV)	Window Thickness (µm)	% Energy Deposited in Window
A	2.5	2	26.1
A	2.5	3	40.5
Proton	2.5	2	2.62
Proton	2.5	3	3.95
Proton	5	2	0.77
Proton	5	3	1.16

4.2.3 Thin Plate Model

The thin plate model was designed to test the effect of the porosity of the plate would effect hydrogen production. The porosity was modeled by altering the volume fraction of water present in the plate. The plate itself was 10 cm square and 80 nm thick.

The thin plate model results showed that the plates with higher plutonium content generated more hydrogen. They also showed that amount of hydrogen that was generated in the water present in the plate was negligible. Table 4.6 shows the data that was gathered in the hydrogen production models for the porous plate source configuration.

Table 4.6: Hydrogen production model results for porous plate configuration. The data was obtained with MCNPX

% H2O	α/s	umol H/s	H molecules/s
30	1.83E+09	0.000245	1.4734E+14
40	1.60E+09	0.000214	1.28822E+14
50	1.37E+09	0.000182	1.0948E+14
60	1.14E+09	0.000151	9.11004E+13
70	8.93E+08	0.00012	7.24132E+13

Figure 4.12 shows the hydrogen production rate as a function of water volume percentage in the porous plate.
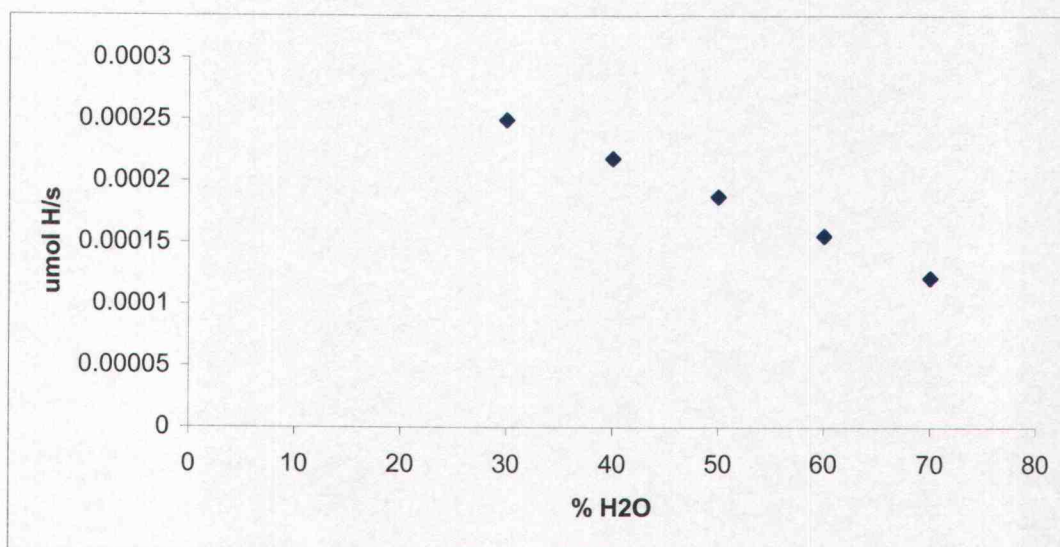
Figure 4.12: Hydrogen production rate as a function of volume % of water in porous plutonium oxide plate

Figure 4.13 shows the hydrogen production rate as a function of distance in water away from a porous plutonium oxide plate.
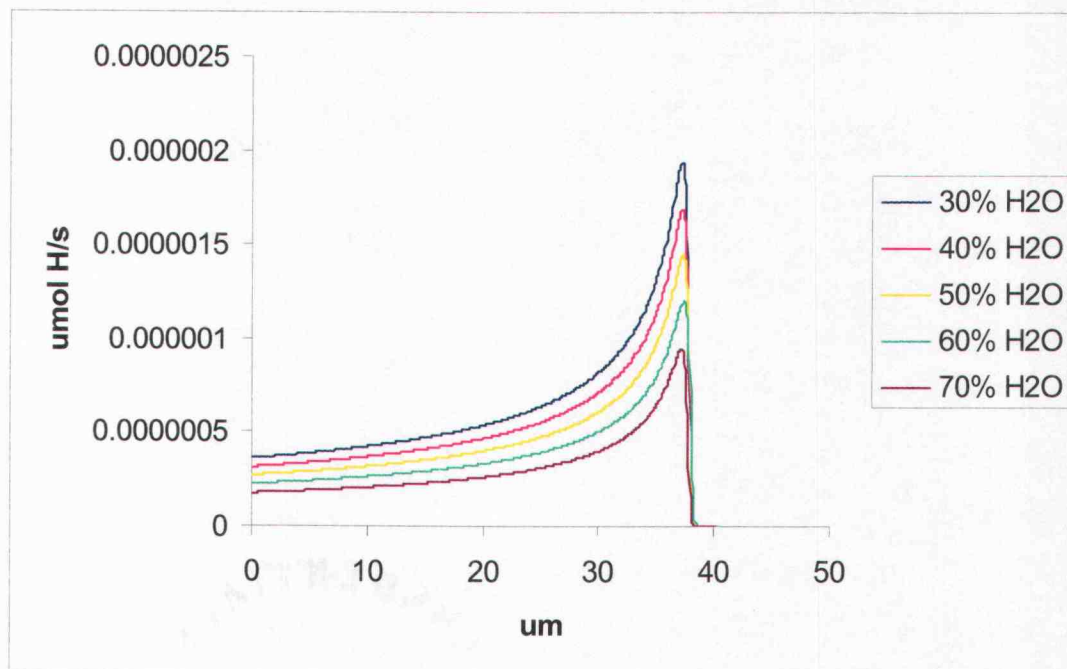
Figure 4.13: Hydrogen production rate as a function of distance in water away from plutonium oxide porous plates with different water percentages

5. Dose Calculations

In this chapter, the radiation dose rate will be studied as it varies with source mass. DARPA has set a guideline stating that the RIMS cell should not cause a dose rate greater than 500 mrem/yr at a distance of 30 cm and set a hard limit at 1000 mrem/yr. Because the RIMS cell uses plutonium oxide as its source, the doses from both α particles and neutrons must be considered.

The model used to simulate the dose rates consisted of a disk of plutonium oxide with a 1 cm diameter and a height that varied depending on the source mass, a water layer 0.09067 cm thick on all sides of the plutonium oxide, and 1.27 cm of steel around the water. Figure 5.1 shows the model geometry. A dose tally surface was placed 30 cm away from the steel's outer surface.
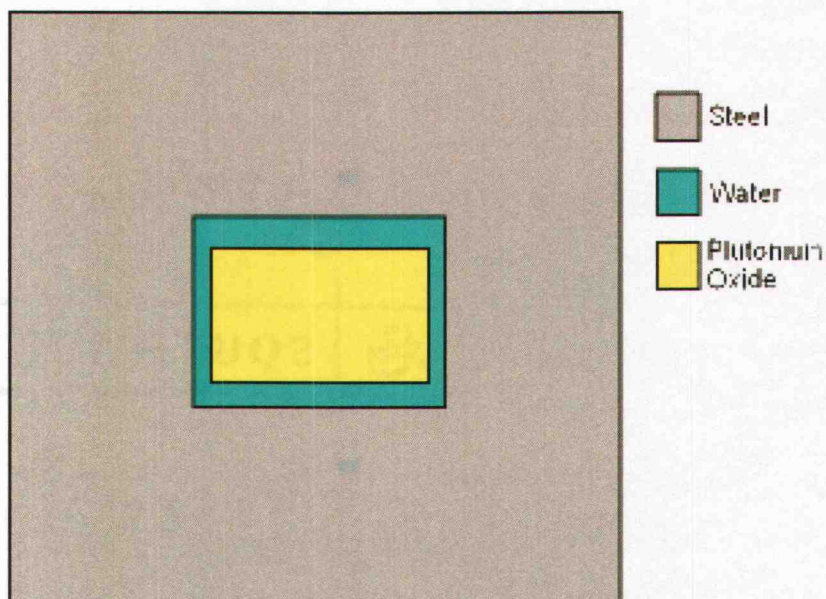
Figure 5.1: Geometry used for MCNPX dose calculations

5.1 α Particle Dose

The dose from α particles was a straight forward calculation. By calculating the mass of plutonium in the oxide disk, an α source strength can be found based on the specific activity of the plutonium isotope. A uniform α source with that source was placed in the volume of the plutonium oxide disk and MCNPX was used to transport the α particles. There were no α particles detected at 30 cm, therefore there was no dose due to α particles.

5.2 Neutron Dose

Unlike α particles, neutrons are secondary radiation from the plutonium oxide. Specifically, the neutrons come from (α,n) reactions with the heavy isotopes of oxygen present in the oxide. Figure 5.2 shows the process used to find the neutron dose from the source disk.
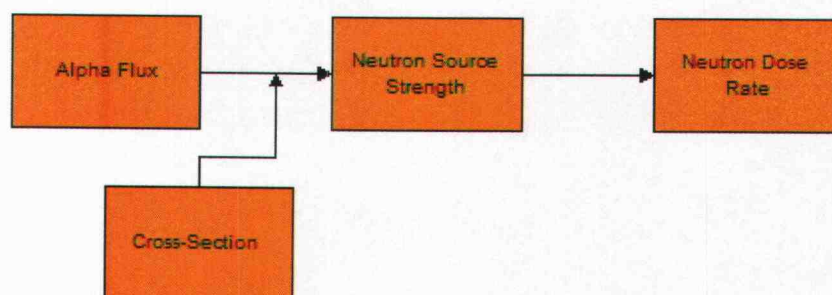
Figure 5.2: Neutron dose methodology

5.2.1 α Flux Calculation

The α flux was found by calculating the α source strength in an identical manner as was described in section 5.1. The α particles were then transported with MCNPX and the flux was tallied within the source disk.

5.2.2 Cross-Section Calculation

The (α,n) cross-section has 2 components: the cross-section for ^{17}O and the

cross-section for ^{18}O. For this simulation, the cross-sections used were taken from the

EXFOR database in the National Nuclear Data Center (NNDC) at Brookhaven

National Laboratory. The cross-sections used were evaluated for α particle energies of

5.5 MeV.

For the purposes of this model, a total macroscopic cross-section was

calculated for plutonium oxide. By taking the natural abundances of ^{17}O and ^{18}O, their

atom density can be found. Their macroscopic cross-sections were calculated by

multiplying their microscopic cross-sections by their atom density. Figure 5.3 shows a

plot of the macroscopic cross-section for the plutonium oxide.
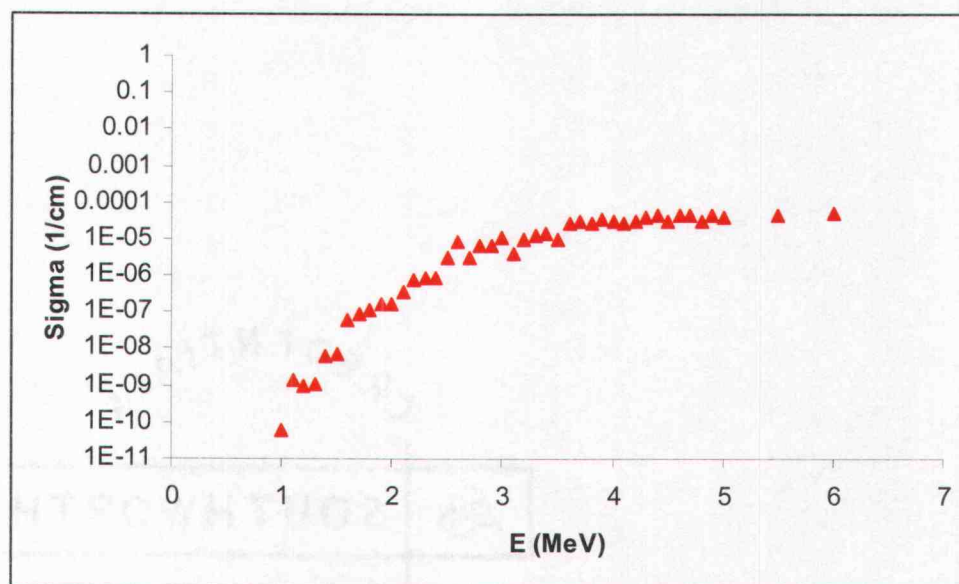
Figure 5.3: Total macroscopic (α,n) cross-section for PuO$_2$

5.2.3 Neutron Source Calculation

The neutron source strength was calculated by multiplying the α flux found in

the MCNPX simulation by the cross-section found in section 5.2.2 and the volume of

the source disk. Figure 5.4 is a plot of the results of the neutron source calculation

with a curve fit applied.

$$y = -0.6813x^3 + 11.018x^2 + 10072x + 29.785$$
$$R^2 = 1$$
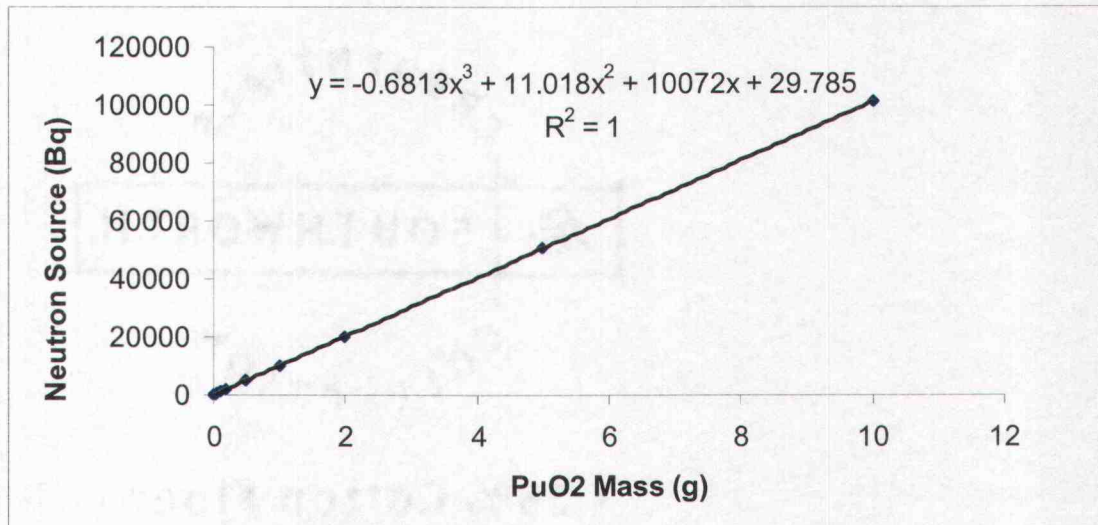
Figure 5.4: Plot of the neutron source strength as a function of source mass

Equation 5.1 gives the formula to find the neutron source strength in

Becquerels as a function of mass of plutonium oxide in grams.

$$A = -0.6813m^3 + 11.018m^2 + 10072m + 29.785 \qquad (5.1)$$

The energy spectrum of the neutron source was taken from a study of 1g of

plutonium oxide that was enriched with plutonium 238 and oxygen 18 (Anderson,

1980). Figure 5.5 is a plot of the neutron energy spectrum.
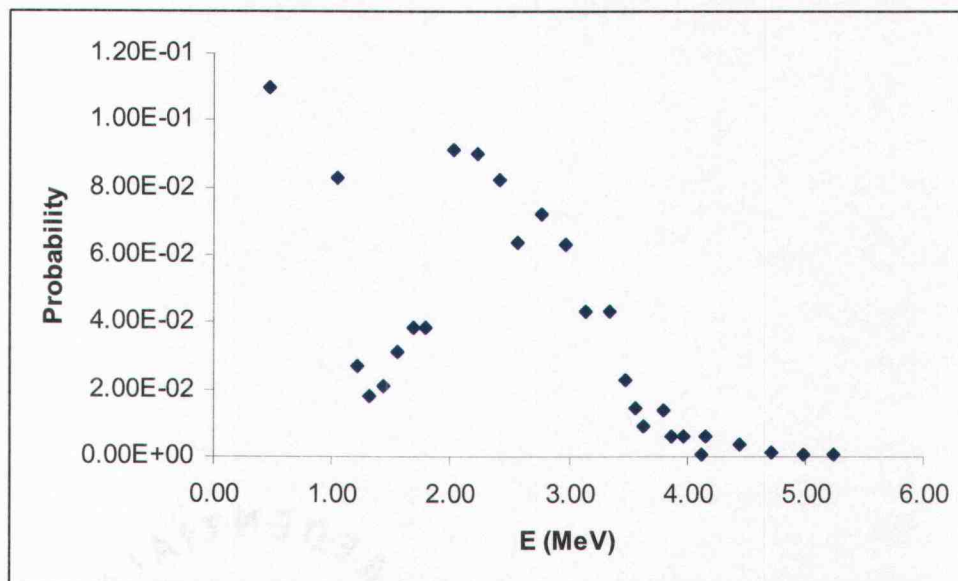
Figure 5.5: Neutron energy spectrum for PuO$_2$

5.2.4 Neutron Dose Calculation

In order to find the neutron dose, MCNPX was used to transport neutrons to the tally surface. The source was defined as a uniform neutron source with the strength that corresponds to the mass of the plutonium oxide that was calculated in section 5.2.3 that was placed in the volume of the plutonium oxide disk. The tally results were multiplied by factors found in ICRP 21 to convert from flux to dose. Figure 5.6 is a plot of the neutron dose as a function of source mass with a curve fit applied.
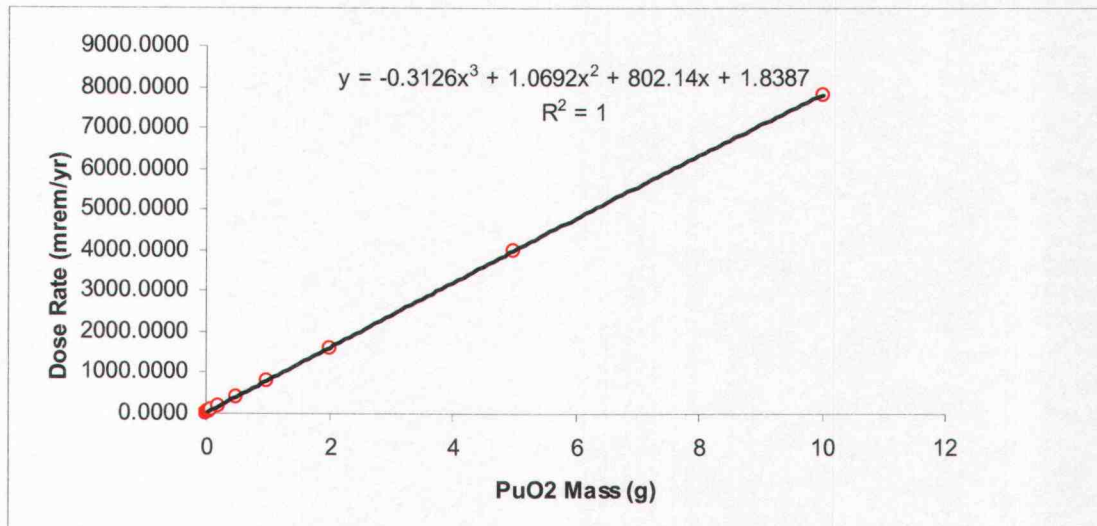
Figure 5.6: Dose rate due to neutrons as a function of source mass

Equation 5.2 is the formula to find the dose rate due to neutrons in mrem/yr as a function of mass of plutonium oxide in grams.

$$\dot{D} = -0.3126m^3 + 1.0692m^2 + 802.14m + 1.8387 \qquad (5.2)$$

Based on Equation 5.2, to meet the 500 mrem/yr guideline the mass limit would be 620 mg of plutonium oxide. To meet the hard limit of 1000 mrem/yr, the mass limit would be 1.24 g.

6. Discussion, Future Work, and Conclusion

The results of the various models used for the RIMS project were helpful for their intended purposes. There were a few problems encountered when it came to the methods used to gather data with MCNPX, but alternative methods were found to provide the information that was needed.

6.1 Source Selection Model

The source selection model clearly illustrated the potential of all of the 13 for generating hydrogen through radiolysis.

The α emitters in general showed greater hydrogen production rates than the β emitters, as was expected based on the literature review and the stopping power. The two isotopes that produced the greatest amount of hydrogen, ^{210}Po and ^{242}Cm, also showed the least favorable performance over time due to their short half-lives.

Of the α emitters, ^{148}Gd, ^{238}Pu, and ^{240}Pu showed the best performance over time due to decay of the source material. ^{240}Pu was not a desirable choice due to its relatively poor hydrogen production potential. The best isotope for hydrogen production of this group was ^{148}Gd, but due to availability, it was decided that ^{238}Pu was the best choice to power the RIMS cell.

When PNNL did the initial calculation of the mass of material required to produce 10 mW, they assumed that all of the power released by radioactive decay would be converted into electricity. By taking the G value of water into account, this

model showed that over an order of magnitude more mass would be required to generate that level of power.

6.2 Accelerator Model

The modeling of the accelerator beam provided a test of using mesh tallies to illustrate hydrogen productions. The graphical output of the mesh data provided information about the range, energy deposition, and divergence of the particle beam.

The range of the α beam was deemed to be too short to be useful for the experiments that needed to be performed, so modeling was done on a proton beam. The proton beam showed similar behavior to that of the α beam, albeit over a larger range. Analysis of the contour plots of the data revealed that the beams remained collimated with very little divergence in the water. The models for both types of particles showed the expected Bragg peak in the stopping power and energy deposition data.

In the analysis, it became clear that the mathematical models were more instructive than the mesh tallies for the particle beams. Since the beams retained their collimation, they could be approximated as 1-dimensional and the Bethe model for stopping power and the fitted function for hydrogen production could then be applied and result in satisfactory values.

6.3 Source Analysis

6.3.1 Particle Size Analysis

The results of the source analysis showed data that is important for optimizing the size of the nanoparticles used as source material for the RIMS cell. The key to the optimization is the minimizing of the self-shielding effect of the plutonium. Self-shielding is the phenomenon of particles being absorbed by the source material before they can exit the material. This leads to only the particles that are emitted in an outer shell of a source contributing to the measured flux of a source that is larger than the range of the particles in that material.

α current and radiated power both increase with diameter. The relationship is cubic, indicating it is driven by the amount of plutonium present in the sphere. Average energy of exiting α particles, however, shows definite self-shielding effects. The trend is linear for the lower end of the diameter range and then is inversely proportional to the square of the diameter. This can be explained by expressing average energy as a function of flux, as in equation 6.1

$$\langle E \rangle = \frac{E\phi}{\phi} \tag{6.1}$$

Flux can be shown to have the nonlinear relationship with radius when the radius becomes greater than the range of the α particle in the medium. This proof is shown in equation 6.2.

$$\phi = \frac{I}{A} = \frac{Act. * \frac{4}{3}\pi(r-R)^3}{4\pi r^2}$$

$$\phi = \frac{Act.}{3}\left[r - 3R + \frac{3R^2}{r} - \frac{R^3}{r^2} \right] \tag{6.2}$$

In equation 6.2, Act is the activity of the source, r is the radius of the sphere, and R is the range of α particles in the medium.

The amount of energy loss in the source material exhibits a cubic relationship to the diameter of the sphere. In order to keep this energy loss to be less than 10%, the nanoparticles should not have diameters greater than 3 μm.

There was a problem encountered in the process of gathering this data with MCNPX. Originally, flux tallies were used and the results were 50% greater than theoretical predictions for volume sources. When a point source of equal activity was put in place of the volume source in identical geometry, the flux tally agreed with the theoretical predictions. After conversations with personnel at LANL, it was found that all MCNP codes have a fundamental error in their surface flux (F2) tallies. If the particles are all traveling parallel to the normal of the tally surface, the results are correct. However, if the particles are not parallel to the normal, the tally will over predict the quantity. To eliminate this problem, the surface flux (F2) tallies were switched to surface outgoing current (F1) tallies.

6.3.2 Particle Spacing Analysis

The particle spacing analysis showed some unexpected results. The main surprise was that the 1 μm and 3 μm particle cases performed almost identically over the same concentrations. The 10 μm particle case performed noticeably better over the range of concentrations, however that must be weighed against the particle self-shielding penalty one gains using a 10 μm particle versus a 3 μm particle.

6.4 Hydrogen Production

The analysis of the thin porous plate showed that the amount of hydrogen produced was primarily driven by the amount of plutonium present in the plate. This was not surprising, because the plate that was modeled was thinner than the range α particles in plutonium oxide and therefore there was very little self-shielding. The relationship between hydrogen production rate and water percentage was roughly linear.

The plate configurations all showed essentially the same distance to the Bragg peak and the same Bragg peak width. Again, the only difference of note was the increase in magnitude that scaled with the amount of plutonium in the plate.

6.5 Future Work

There is further work to be done on the system modeling of the RIMS cell. This research examined the process of hydrogen production and the optimization of the source geometry. However, it did not study the flow of hydrogen to the fuel cell and the generation of electricity in that cell.

The transport of the hydrogen through plates that have different percentages of water by volume will need to be performed to truly optimize the porosity of the source plate. To provide a more accurate model of a plate that may be used in the RIMS cell, a code for a stochastic mixture would provide a realistic results than the homogeneous mixture that was modeled in MCNPX. The percentage of hydrogen that is produced

that actually reaches the fuel cell is also critical in accurately gauging the electrical production of the cell.

Another area of future work is the study of other substances than water that could be used as a medium for radiolysis. If a suitable material is found with a lower G value than that of water, the increase of hydrogen production should create a greater power output. The lower G value has to be weighed against the corrosiveness of the other materials as to not lessen the lifetime of the RIMS cell in a significant manner.

6.6 Conclusion

This study has answered many important questions for the OSU RIMS project. The source material was chosen in part based on these results. The validity of using a particle accelerator to simulate radiolysis was confirmed based on the models developed in this study. Perhaps most importantly, this research has provided the investigators of the RIMS project an insight on how the source configuration can affect the process of radiolysis.

BIBLIOGRAPHY

Allen, A.O., *"The Radiation Chemistry of Water and Aqueous Solutions,"* Text, D. Van Nostrand, 1961.

Krane, K. S., *"Introductory Nuclear Physics,"* Text, John Wiley & Sons, 1988.

Vinson, D. W., Deible, R. W., and Sindelar, R. L., *"Evaluation of Hydrogen Generation from Radiolysis from Breached Spent Fuel,"* Westinghouse Savannah River Company, Aiken, SC, Report # WSRC-MS-2002-00728 (2002).

Hart, E. J., McDonell, W. R., and Gordon, S., *"The Decomposition of Light and Heavy Water Boric Acid Solutions by Nuclear Reactor Radiations,"* Proceedings of the International Conference on the Peaceful Uses of Atomic Energy, Geneva 1955, Vol. 7, p. 593, United Nations, New York (1956).

Dolin, P. I. and Ershler, B. V., *"Radiolysis of Water in the Presence of H2 and O2 due to Reactor Radiation, Fission Fragments and X-Radiation,"* Proceedings of the International Conference on the Peaceful Uses of Atomic Energy, Geneva 1955, Vol. 7, p. 564, United Nations, New York (1956).

Crawford, C. L. and Bibler, N. E., '*Hydrogen Production in Radioactive Solutions in the Defense Waster Processing Facility,"* Westinghouse Savannah River Company, Aiken, SC, Report # WSRC-TR-95-0090 (1995)

L. S. Waters, ed., *"MCNPX User's Manual, Version 2.3.0,"* LA-UR-02-2607 (April 2002)

Anderson, Edward M., *"Neutron Energy Spectra of a 238Pu—18O(α,n) Source—Unmoderated and Polyethylene Moderated".* Health Physics, vol 39, pp 537-542. 1980

APPENDICES

Appendix A: Input Files

The following input file is for a 2.5 MeV α beam case in the CWRU

accelerated. This case had a 2 μm SiC window. The quantities tallied in this

simulation were α flux, α population, stopping power, and total energy deposition.

The mesh tallies only cover a quarter of the beam for visualization purposes.

```
Accelerator Window (2 micron) Model, 2.5 MeV Alpha
c Cells
11 1 -3.21 11 -12 13 -14 15 -16 imp:a=1 $SiC Window
21 0     -11 21 13 -14 15 -16 imp:a=0 $Void
22 0     12 -22 13 -14 15 -16 imp:a=0 $Void
23 0     -13 23 15 -16      imp:a=0 $Void
24 0     14 -24 15 -16      imp:a=0 $Void
25 0     -15 23 -24         imp:a=0 $Void
31 2 -1   21 -22 23 -24 16 -26 imp:a=1 $Water Cell
41 0     -21 23 -24 16 -26   imp:a=0 $Void
42 0     22 23 -24 16 -26    imp:a=0 $Void
43 0     -23 -26            imp:a=0 $Void
44 0     24 -26            imp:a=0 $Void
45 0     26               imp:a=0 $Void

c Surface Cards
11 px -.1
12 px .1
13 py -.1
14 py .1
15 pz  0
16 pz .0002
21 px -.2
22 px .2
23 py -.2
24 py .2
26 pz .004

c Material Cards
m1 14000 .5 6000 .5 $Silicon Carbide
m2 1001 .667 8016 .333 $Water
c Data Cards
mode a $Transport alpha particles
CUT:a J .1 $Set lower energy cut off at .1 MeV
TMESH
RMESH11:a flux $Rectangular alpha flux mesh tally
CORA11 -.15 -.145 -.14 -.135 -.13 -.125 -.12 -.115 -.11 -.105
     -.1 -.095 -.09 -.085 -.08 -.075 -.07 -.065 -.06 -.055 -.05 -.045
     -.04 -.035 -.03 -.025 -.02 -.015 -.01 -.005 0
CORB11 -.15 -.145 -.14 -.135 -.13 -.125 -.12 -.115 -.11 -.105
     -.1 -.095 -.09 -.085 -.08 -.075 -.07 -.065 -.06 -.055 -.05 -.045
     -.04 -.035 -.03 -.025 -.02 -.015 -.01 -.005 0
CORC11 0 0.0001 .0002 .0003 .0004 .0005 .0006 .0007 .0008 .0009 .001
     .0011 .0012 .0013 .0014 .0015 .0016 .0017 .0018 .0019 .002 .0021
```

```
       .0022 .0023 .0024 .0025 .0026 .0027 .0028 .0029 .003 .003025 .00305
       .003075 .0031  .003125 .00315 .003175 .0032 .003225 .00325 .003275
       .0033 .003325 .00335 .003375 .0034 .003425 .00345 .003475 .0035
       .003525 .00355 .003575 .0036  .003625 .00365 .003675 .0037 .003725
       .0038 .003825 .00385 .003875  .0039 .003925 .00395 .003975 .004
RMESH21:a popul $Rectangular alpha population mesh tally
CORA21 -.15 -.145 -.14 -.135 -.13 -.125 -.12 -.115 -.11 -.105
       -.1 -.095 -.09 -.085 -.08 -.075 -.07 -.065 -.06 -.055 -.05 -.045
       -.04 -.035 -.03 -.025 -.02 -.015 -.01 -.005 0
CORB21 -.15 -.145 -.14 -.135 -.13 -.125 -.12 -.115 -.11 -.105
       -.1 -.095 -.09 -.085 -.08 -.075 -.07 -.065 -.06 -.055 -.05 -.045
       -.04 -.035 -.03 -.025 -.02 -.015 -.01 -.005 0
CORC21 0 0.0001 .0002 .0003 .0004 .0005 .0006 .0007 .0008 .0009 .001
       .0011 .0012 .0013 .0014 .0015 .0016 .0017 .0018 .0019 .002 .0021
       .0022 .0023 .0024 .0025 .0026 .0027 .0028 .0029 .003 .003025 .00305
       .003075 .0031  .003125 .00315 .003175 .0032 .003225 .00325 .003275
       .0033 .003325 .00335 .003375 .0034 .003425 .00345 .003475 .0035
       .003525 .00355 .003575 .0036  .003625 .00365 .003675 .0037 .003725
       .0038 .003825 .00385 .003875  .0039 .003925 .00395 .003975 .004
RMESH13 de/dx $Rectangular stopping power tally
CORA13 -.15 -.145 -.14 -.135 -.13 -.125 -.12 -.115 -.11 -.105
       -.1 -.095 -.09 -.085 -.08 -.075 -.07 -.065 -.06 -.055 -.05 -.045
       -.04 -.035 -.03 -.025 -.02 -.015 -.01 -.005 0
CORB13 -.15 -.145 -.14 -.135 -.13 -.125 -.12 -.115 -.11 -.105
       -.1 -.095 -.09 -.085 -.08 -.075 -.07 -.065 -.06 -.055 -.05 -.045
       -.04 -.035 -.03 -.025 -.02 -.015 -.01 -.005 0
CORC13 0 0.0001 .0002 .0003 .0004 .0005 .0006 .0007 .0008 .0009 .001
       .0011 .0012 .0013 .0014 .0015 .0016 .0017 .0018 .0019 .002 .0021
       .0022 .0023 .0024 .0025 .0026 .0027 .0028 .0029 .003 .003025 .00305
       .003075 .0031  .003125 .00315 .003175 .0032 .003225 .00325 .003275
       .0033 .003325 .00335 .003375 .0034 .003425 .00345 .003475 .0035
       .003525 .00355 .003575 .0036  .003625 .00365 .003675 .0037 .003725
       .0038 .003825 .00385 .003875  .0039 .003925 .00395 .003975 .004
RMESH23 total $Rectangular energy deposition mesh tally
CORA23 -.15 -.145 -.14 -.135 -.13 -.125 -.12 -.115 -.11 -.105
       -.1 -.095 -.09 -.085 -.08 -.075 -.07 -.065 -.06 -.055 -.05 -.045
       -.04 -.035 -.03 -.025 -.02 -.015 -.01 -.005 0
CORB23 -.15 -.145 -.14 -.135 -.13 -.125 -.12 -.115 -.11 -.105
       -.1 -.095 -.09 -.085 -.08 -.075 -.07 -.065 -.06 -.055 -.05 -.045
       -.04 -.035 -.03 -.025 -.02 -.015 -.01 -.005 0
CORC23 0 0.0001 .0002 .0003 .0004 .0005 .0006 .0007 .0008 .0009 .001
       .0011 .0012 .0013 .0014 .0015 .0016 .0017 .0018 .0019 .002 .0021
       .0022 .0023 .0024 .0025 .0026 .0027 .0028 .0029 .003 .003025 .00305
       .003075 .0031  .003125 .00315 .003175 .0032 .003225 .00325 .003275
       .0033 .003325 .00335 .003375 .0034 .003425 .00345 .003475 .0035
       .003525 .00355 .003575 .0036  .003625 .00365 .003675 .0037 .003725
       .0038 .003825 .00385 .003875  .0039 .003925 .00395 .003975 .004
ENDMD
c Define a 2.5 MeV, 100 nA alpha beam source
SDEF ERG=2.5 WGT=3.125E11 SUR=15 POS=0 0 0  RAD=d1 DIR=1 PAR=34
SI1  0 .1
NPS 20000000 $Run 20000000 particles
```

The following input file is similar to the previous one, except the beam is protons instead of α particles. The quantities tallied are proton flux, stopping power, and energy deposition.

```
Accelerator Window (2 micron) Model, 2.5 MeV Proton
c Cells
11 1 -3.21 11 -12 13 -14 15 -16 imp:h=1 $SiC Window
21 0     -11 21 13 -14 15 -16 imp:h=0 $Void
22 0     12 -22 13 -14 15 -16 imp:h=0 $Void
23 0     -13 23 15 -16     imp:h=0 $Void
24 0     14 -24 15 -16     imp:h=0 $Void
25 0     -15 23 -24     imp:h=0 $Void
31 2 -1    21 -22 23 -24 16 -26 imp:h=1 $Water Cell 1
c 32 2 -1   21 -22 23 -24 25 -26 imp:h=1 $Water Cell 2
41 0     -21 23 -24 16 -26   imp:h=0 $Void
42 0     22 23 -24 16 -26   imp:h=0 $Void
43 0     -23 -26     imp:h=0 $Void
44 0     24 -26     imp:h=0 $Void
45 0     26     imp:h=0 $Void

c Surface Cards
11 px -.1
12 px .1
13 py -.1
14 py .1
15 pz  0
16 pz .0002
21 px -.2
22 px .2
23 py -.2
24 py .2
26 pz .0152

c Material Cards
m1 14000 .5 6000 .5 $Silicon Carbide
m2 1001 .667 8016 .333 $Water
c Data Cards
mode h $Transport protons
CUT:h J .1 $Set lower energy cutoff at .1 MeV
TMESH
RMESH11:h flux $Rectangular proton flux mesh tally
CORA11 -.15 -.145 -.14 -.135 -.13 -.125 -.12 -.115 -.11 -.105
     -.1 -.095 -.09 -.085 -.08 -.075 -.07 -.065 -.06 -.055 -.05 -.045
     -.04 -.035 -.03 -.025 -.02 -.015 -.01 -.005 0
CORB11 -.15 -.145 -.14 -.135 -.13 -.125 -.12 -.115 -.11 -.105
     -.1 -.095 -.09 -.085 -.08 -.075 -.07 -.065 -.06 -.055 -.05 -.045
     -.04 -.035 -.03 -.025 -.02 -.015 -.01 -.005 0
CORC11 0 .0002 .0012 .0022 .0032 .0042 .0052 .0062 .0072 .0082 .0092 .0102
     .0112 .0122 .0132 .0142 .0152
RMESH13 de/dx $Rectangular stopping power mesh tally
CORA13 -.15 -.145 -.14 -.135 -.13 -.125 -.12 -.115 -.11 -.105
     -.1 -.095 -.09 -.085 -.08 -.075 -.07 -.065 -.06 -.055 -.05 -.045
     -.04 -.035 -.03 -.025 -.02 -.015 -.01 -.005 0
```

```
CORB13 -.15 -.145 -.14 -.135 -.13 -.125 -.12 -.115 -.11 -.105
      -.1 -.095 -.09 -.085 -.08 -.075 -.07 -.065 -.06 -.055 -.05 -.045
      -.04 -.035 -.03 -.025 -.02 -.015 -.01 -.005 0
CORC13 0 .0002 .0012 .0022 .0032 .0042 .0052 .0062 .0072 .0082 .0092 .0102
      .0112 .0122 .0132 .0142 .0152
RMESH23 total $Rectangular energy deposition mesh tally
CORA23 -.15 -.145 -.14 -.135 -.13 -.125 -.12 -.115 -.11 -.105
      -.1 -.095 -.09 -.085 -.08 -.075 -.07 -.065 -.06 -.055 -.05 -.045
      -.04 -.035 -.03 -.025 -.02 -.015 -.01 -.005 0
CORB23 -.15 -.145 -.14 -.135 -.13 -.125 -.12 -.115 -.11 -.105
      -.1 -.095 -.09 -.085 -.08 -.075 -.07 -.065 -.06 -.055 -.05 -.045
      -.04 -.035 -.03 -.025 -.02 -.015 -.01 -.005 0
CORC23 0 .0002 .0012 .0022 .0032 .0042 .0052 .0062 .0072 .0082 .0092
      .0102 .0112 .0122 .0132 .0142 .0152
ENDMD
c Define a 2.5 MeV, 100 nA proton beam source
SDEF ERG=2.5 WGT=6.25E11 SUR=15 POS=0 0 0  RAD=d1  DIR=1 PAR=9
SI1  0 .1
NPS 2000000 $Run 2000000 particles
```

The following input file was used for the nanoparticle analysis. This particular file modeled a 20 nm PuO_2 sphere. The asterix before tally F11 denotes that it is tallying an energy current rather than a particle current.

```
Plutonium Sphere Measurement (20 nm diameter)
c Cell Cards
1 1 -11.46 -1 imp:a=1 $Plutonium oxide sphere
2 0       1 imp:a=0 $Void

c Surface Cards
1 so 10E-7

c Data Cards
m1 94238 .3333 8016 .6667 $Plutonium Oxide
mode a $Transport alphas
CUT:a J .1 $Set lower energy cut off at .1 MeV
c Define alpha source based on Pu238 data
SDEF RAD=d1 POS=0 0 0 ERG=5.5 WGT=2.65E-5 PAR=34
SI1 0 10E-7
SP1 -21 2
*F11:a 1.2 $Exiting alpha power
F21:a 1.2 $Exiting alpha current
F16:a 1 $Energy deposited by alphas in the sphere per unit mass
FM16 4.80035E-17 $Multiply above tally by sphere mass
NPS 10000 $Run 10000 particles
```

The following input file was used to model on of the porous plate source cases for the RIMS cell. The quantities tallied were energy current, α current, and energy deposition in the plate.

```
Porous Plate Model, 40% H20
c Cell Cards
1 1 -7.384 -1 imp:a=1 $Plutonium oxide plate
2 0      1 imp:a=0 $Void

c Surface Cards
1 rpp 0 10 0 10 0 8.06E-6

c Data Cards
m1 1001 .308 8016 .513 94238 .179 $Plutonium oxide mixed w/ water
mode a $Transport alphas
CUT:a J .1 $Set lower energy cut off at .1 MeV
c Define alpha source in the plate based on Pu238 data
SDEF x=d1 y=d2 z=d3 ERG=5.49 WGT=3.23E9 PAR=34
SI1 0 10
SP1 0 1
SI2 0 10
SP2 0 1
SI3 0 8.06E-6
SP3 0 1
*F11:a 1.2 $Exiting alpha power on the upper surface of the plate
F21:a 1.2 $Exiting alpha current on the upper surface of the plate
F16:a 1 $Energy deposited by alphas in the plate per unit mass
FM16 5.95E-3 $Multiply the above tally by the mass of the plate
NPS 100000 $Run 100000 particles
```

Appendix B: HYPR Description

While TecPlot could be used to display the output from the mesh tallies, it did not allow for some key features that were either required or desirable to reach the research objectives. The first problem was that it did not allow for two data files to be convolved with each other to obtain a new quantity. Since hydrogen production requires the multiplication of the G value, derived from the stopping power data, and the energy deposition data, it was imperative that a solution be found. The other deficiency in TecPlot is its the inability to display more than one cut plane at a time.

The solution to these problems was to generate a new display program that fit the needs of the research. The new program, called HYPR, was developed in C++ using OpenGL to create the graphical display.

To prepare the TecPlot data files for use in HYPR, the header section of the file must be deleted so that only the five data columns remain. The names of the data files and the mesh data of the files are input into the constants section of the HYPR code.

HYPR reads in the data from the stopping power data file and converts it to G value by using the G value equation. The data from the energy deposition file is then read in and then multiplied by the G value data to get the hydrogen production values. The point data obtained in this method are then assigned colors on a blue-green-red scale based on their value relative to the maximum and minimum values of the data. The points are displayed in 3-Dimensional space, where the user can scale, rotate, and translate it.

HYPR incorporates range sliders, OpenGL technology developed at the University of California at Santa Barbara. Range sliders are similar to regular sliders, only a range of data can be set and that window can be slid between the minimum and maximum data values. The values that range sliders control in HYPR are x, y, z, and hydrogen production.

HYPR incorporates three orthogonal cutting planes. The three planes can be displayed on at a time or in any combination with each other. There are two settings for the cutting planes: shaded and contour. Shaded planes provide a solid view of the colors representing the hydrogen production values in the plane. Contour planes show a number of contour lines that can be set by a spinner in the interface window. Figures B1 and B2 show shaded and contour planes in HYPR, respectively.
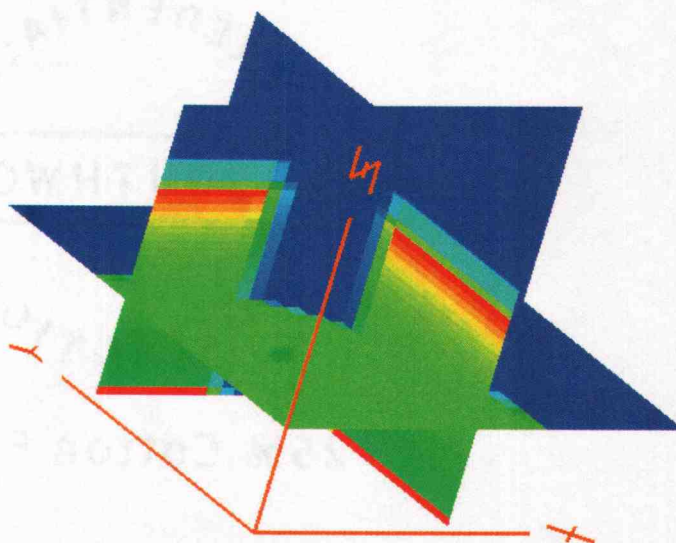
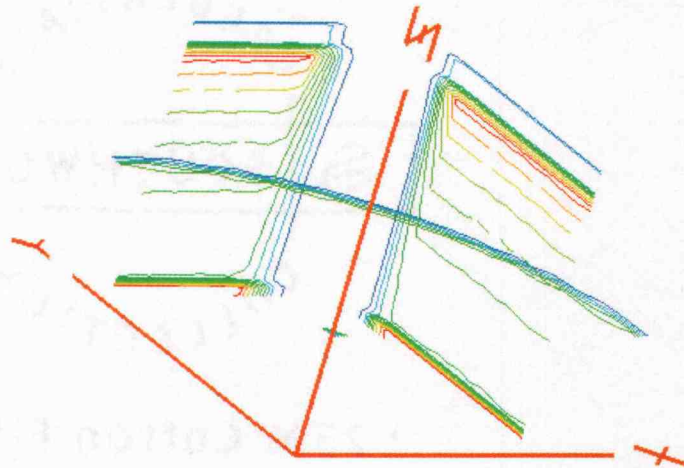

Figure B1: Shaded cut planes in HYPR

Figure B2: Contour cut planes in HYPR

Another feature of HYPR is the inclusion of wire-frame isosurfaces. The value of the isosurface can be input via a spinner in the HYPR interface window. The program finds each point that has the desired values in a series of x, y, and z planes and connects the points, giving the appearance of a wire-frame 3-D surface. Figure B3 show an isosurface created in HYPR. Currently only one isosurface can be displayed at a time but the code can be adapted to allow multiple isosurfaces.
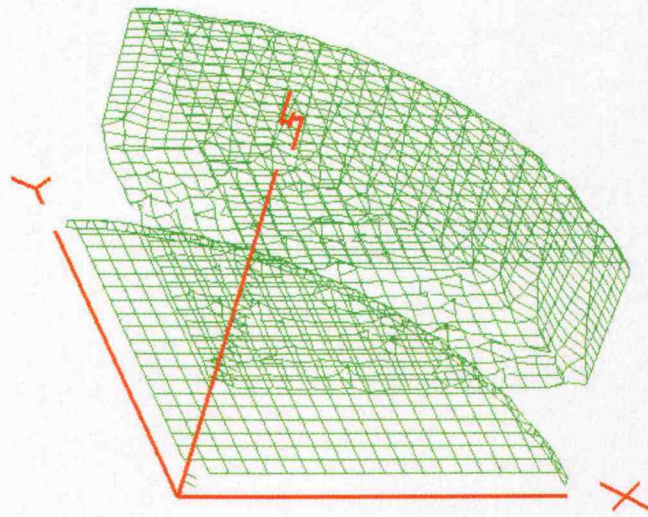
Figure B3: Isosurface in HYPR